Current Biology

Report

Ase1 selectively increases the lifetime of antiparallel microtubule overlaps

Highlights

- Ase1 can significantly enhance the lifetime of antiparallel microtubule overlaps
- Ase1 selectively promotes rescues for antiparallelly crosslinked microtubules
- Ase1 is herded by depolymerizing microtubule ends
- Ase1 herding correlates with reduced microtubule depolymerization speed

Authors

Jochen Krattenmacher,
Manuel Lera-Ramirez,
Alexandre Beber, ..., Stefan Diez,
Marcus Braun, Zdenek Lansky

Correspondence

marcus.braun@ibt.cas.cz (M.B.),
zdenek.lansky@ibt.cas.cz (Z.L.),
stefan.diez@tu-dresden.de (S.D.),
fjn28@cam.ac.uk (F.N.)

In brief

Krattenmacher et al. demonstrate that the microtubule (MT) crosslinker Ase1 selectively impedes the depolymerization of MTs in antiparallel overlaps, with lesser effects on parallel and isolated MTs. They also show that Ase1 is herded by depolymerizing MT ends, and that this herding correlates with reduced MT depolymerization speed.

Krattenmacher et al., 2024, Current Biology *34*, 4071–4080
September 9, 2024
https://doi.org/10.1016/j.cub.2024.07.055

CellPress

Current Biology

CellPress
OPEN ACCESS

Report

Ase1 selectively increases the lifetime of antiparallel microtubule overlaps

Jochen Krattenmacher,[1,2,3] Manuel Lera-Ramirez,[4] Alexandre Beber,[1] Stepan Herynek,[1] Lenka Grycova,[1] Xiaocheng Liu,[5] Pavel Neuzil,[5] Francois Nedelec,[6,*] Stefan Diez,[2,7,8,*] Marcus Braun,[1,*] and Zdenek Lansky[1,9,*]

[1]Institute of Biotechnology, Czech Academy of Sciences, BIOCEV, 25250 Vestec, Czechia
[2]B CUBE - Center of Molecular Bioengineering, Technische Universität Dresden, 01307 Dresden, Germany
[3]Faculty of Science, Charles University in Prague, 12800 Prague, Czech Republic
[4]Institut Curie, PSL Research University, Sorbonne Université, CNRS UMR144, Paris, France
[5]School of Mechanical Engineering, Department of Microsystem Engineering, Northwestern Polytechnical University, Xi'an, Shaanxi 710072, P.R. China
[6]Sainsbury Laboratory Cambridge, University of Cambridge, CB2 1LR Cambridge, UK
[7]Max Planck Institute of Molecular Cell Biology and Genetics, 01307 Dresden, Germany
[8]Cluster of Excellence Physics of Life, Technische Universität Dresden, 01062 Dresden, Germany
[9]Lead contact
*Correspondence: marcus.braun@ibt.cas.cz (M.B.), zdenek.lansky@ibt.cas.cz (Z.L.), stefan.diez@tu-dresden.de (S.D.), fjn28@cam.ac.uk (F.N.)
https://doi.org/10.1016/j.cub.2024.07.055

SUMMARY

Microtubules (MTs) are dynamically unstable polar biopolymers switching between periods of polymerization and depolymerization, with the switch from the polymerization to the depolymerization phase termed catastrophe and the reverse transition termed rescue.[1] In presence of MT-crosslinking proteins, MTs form parallel or anti-parallel overlaps and self-assemble reversibly into complex networks, such as the mitotic spindle. Differential regulation of MT dynamics in parallel and anti-parallel overlaps is critical for the self-assembly of these networks.[2,3] Diffusible MT crosslinkers of the Ase1/MAP65/PRC1 family associate with different affinities to parallel and antiparallel MT overlaps, providing a basis for this differential regulation.[4–11] Ase1/MAP65/PRC1 family proteins directly affect MT dynamics[12] and recruit other proteins that locally alter MT dynamics, such as CLASP or kinesin-4.[7,13–16] However, how Ase1 differentially regulates MT stability in parallel and antiparallel bundles is unknown. Here, we show that Ase1 selectively promotes antiparallel MT overlap longevity by slowing down the depolymerization velocity and by increasing the rescue frequency, specifically in antiparallelly crosslinked MTs. At the retracting ends of depolymerizing MTs, concomitant with slower depolymerization, we observe retention and accumulation of Ase1 between crosslinked MTs and on isolated MTs. We hypothesize that the ability of Ase1 to reduce the dissociation of tubulin subunits is sufficient to promote its enrichment at MT ends. A mathematical model built on this idea shows good agreement with the experiments. We propose that differential regulation of MT dynamics by Ase1 contributes to mitotic spindle assembly by specifically stabilizing antiparallel overlaps, compared to parallel overlaps or isolated MTs.

RESULTS AND DISCUSSION

Ase1 selectively promotes the persistence of antiparallel microtubule overlaps

To study the interactions of Ase1 and dynamic microtubules (MTs), we employed total internal reflection fluorescence (TIRF) and interference reflection microscopy (IRM) time-lapse imaging of immobilized, GMPCPP-stabilized MT seeds in the presence of free tubulin (30 μM) and fluorescently labeled Ase1 (10, 42, and 420 nM) (STAR Methods). We observed dynamic, Ase1-decorated MT extensions polymerizing from the MT seeds. When a polymerizing MT plus end encountered another MT, it either crossed the other MT or formed a bundle with it (Figures 1A, 1B, and S1A; Videos S1A–S1F), depending on the angle of incidence and Ase1 concentration (Figure S1B). As previously reported,[6] antiparallel bundles formed even at large initial angles of incidence (up to 40° at higher Ase1 concentrations), while parallel bundles mostly formed at initial angles below 20° (Figure S1B). In the absence of Ase1, MTs never bundled, even when very close to each other over extended periods of time (Figure S1C; Video S1G). We then quantified the lifetimes of parallel and antiparallel overlaps in these experiments. Although at 10 nM Ase1 we found that antiparallel overlaps were no more stable than parallel ones (Figure 1C), with increasing Ase1 concentration a difference between the lifetimes increased, with antiparallel overlaps having higher lifetimes (Figure 1C). We

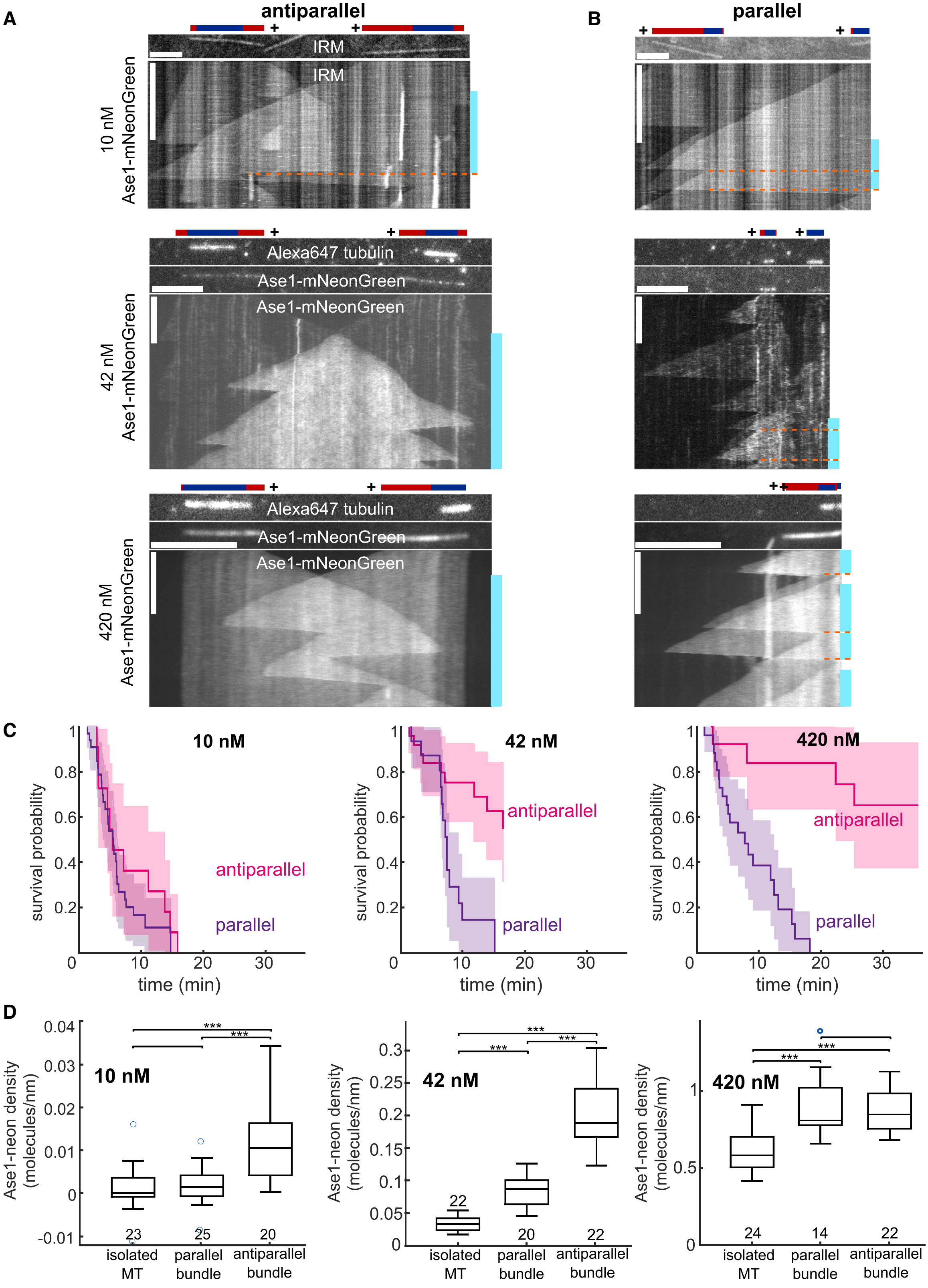

Figure 1. Ase1 selectively promotes the persistence of antiparallel MT overlaps

(A) Kymographs of two MTs polymerizing toward each other in the presence of Ase1-mNeonGreen, subsequently forming a region of antiparallel MT overlap (scale bars, 5 μm and 10 min). In sketches, dynamic extensions with GDP lattices are red and stabilized GMPCPP seeds are blue. The teal bars next to

(legend continued on next page)

hypothesized that this effect could be due to increased densities of Ase1 molecules bound in antiparallel overlaps compared to parallel ones, as reported earlier.[6] Indeed, with 10 and 42 nM Ase1 in solution, the observed Ase1 densities on antiparallel overlaps were much higher than on parallel ones (Figure 1D). At 420 nM Ase1, we observed the density of Ase1 to be similar to Ase1 densities on antiparallel and parallel bundles (Figure 1D). The measured values, however, represent the total density of Ase1 at the position of the overlap, which might differ from the density of Ase1 molecules directly engaged in MT crosslinking by being bound simultaneously to both MTs. Importantly, despite similar decoration levels by Ase1 at 420 nM, antiparallel overlaps nevertheless were significantly more stable than parallel ones (Figure 1C). Combined, these data show that Ase1 selectively promotes the lifetimes of antiparallel overlaps.

Ase1 differentially regulates the dynamics of microtubules in parallel and antiparallel overlaps

The relative stability of antiparallel overlaps at high Ase1 concentrations may, in part, owe to the fact that antiparallel overlaps grow twice as fast as parallel ones, since both MTs polymerize in opposite directions. However, our data suggest that antiparallel overlaps may be additionally stabilized by altered MT dynamics. To investigate this question, we quantified MT dynamics for various Ase1 concentrations (Figures 2 and S2A). We found that polymerization velocities were similar for all MTs, either isolated or bundled, across all tested Ase1 concentrations (Figure 2A). The catastrophe frequencies slightly decreased with Ase1 concentration similarly in isolated or bundled MTs (Figure 2B). Importantly, we found both depolymerization velocities and rescue frequencies to be sensitive to both Ase1 concentration and the MT organization (Figures 2C and 2D). At 420 nM Ase1, MTs depolymerized markedly slower than at lower Ase1 concentrations. Further, at 42 and 420 nM Ase1, antiparallel MTs displayed a marked decrease in depolymerization velocity and a pronounced increase in rescue frequency compared to isolated and parallel MTs (Figures 2C and 2D). Our results at 42 nM Ase1 may indicate that this effect is due to the increased number of Ase1 molecules observed on antiparallel MTs as compared to parallel and isolated MTs. At 420 nM Ase1, however, the decrease in depolymerization velocities and pronounced increase in rescue frequencies persist despite indistinguishable Ase1 densities on antiparallel versus parallel MT overlaps (Figures 2E and 2F). The number of Ase1 molecules localized to the MT overlap was the only factor we could identify as influencing the frequency of rescues (Figures 2D and 2F). Note, however, that the number of molecules directly participating in the crosslinking process, i.e., simultaneously bound to both crosslinked MTs, is not measurable in this assay. Combined, these results demonstrate that Ase1 can differently modulate MT dynamics in parallel and antiparallel overlaps, resulting in stabilization of antiparallel MT overlaps.

Slower MT depolymerization coincides with accumulation of Ase1 at depolymerizing MT ends

To investigate the mechanism underpinning Ase1-dependent MT stabilization, we next examined the localization of Ase1 on MTs. Although on polymerizing MTs Ase1 did not exhibit any specific localization, on depolymerizing MTs, we observed that Ase1 accumulated at MT ends (Figures 1 and S2B). We thus repeated the experiments at a higher frame rate and altered experimental conditions to analyze this process (STAR Methods; Figures S3A and S3B). We had chosen an Ase1 concentration (1 nM) at which we observed very little Ase1 binding to isolated MTs while observing prominent binding to antiparallel overlaps (Figures 3A, 3D, and S3C; Video S2). At the depolymerizing ends of overlaps and isolated MTs, we observed accumulation of Ase1 molecules (Figures 3A, 3B, and S3D). We found that as Ase1 accumulated at the disassembling tip, the velocity of the MT disassembly decreased for both, for overlaps and isolated MTs (Figures 3A–3F and S3E). We next compared Ase1 accumulation at the ends of antiparallel overlaps and isolated MTs, after adjusting the bulk Ase1 concentrations to reach comparable Ase1 densities on the MTs. This was achieved by imaging antiparallel overlaps at 1 nM Ase1 and isolated MTs at 6 nM Ase1 (Figures 3G and S3C). We found that although isolated MTs at 6 nM Ase1 accumulated more Ase1 than antiparallel MTs at 1 nM Ase1, these isolated MTs did not depolymerize slower than the antiparallel MTs at 1 nM (Figures 3B, 3C, 3H, and 3I). While recent results indicate that gradual slowdown of disassembly is an inherent feature of MT depolymerization,[17] in the absence of Ase1 we had not observed any slowdown in MT depolymerization comparable to what we observed in the presence of Ase1 (Figures S3F and S3G). Moreover, we found that with an increasing amount of accumulated Ase1 at the MT tip, as well as with an overall increase in local density of Ase1 molecules at the tip, the probability of rescue increased (Figures 3A–3J and S3H). We repeated the experiment with both Ase1 and tubulin removed from the solution. As MTs started to depolymerize, Ase1 still accumulated at the depolymerizing ends, indicating that the accumulates are composed of Ase1 molecules that were already bound to the MT lattice before catastrophe (Figure S3I; Video S3). As recently reported with a synthetic MT crosslinker,[18] we also observed that a depolymerizing MT end would drag other MTs, indicating that substantial forces could be transmitted by this mechanism (Figure S3J; Video S3). In summary, our experiments demonstrate that lattice-bound Ase1 molecules are swept by the depolymerizing MT ends and that the number of swept Ase1 molecules correlates with reduced depolymerization velocity and increased rescue probability.

kymographs indicate the presence of regions of overlap (we only counted regions where the two partaking MT regions are constituted by GDP-tubulin, i.e., a seed stabilized by GMPCPP did not count). The orange lines indicate a termination of the overlapping period, as evaluated for (C).

(B) Kymographs of two MTs polymerizing in a parallel configuration in the presence of Ase1-mNeonGreen, sometimes forming a region of overlap.

(C) Survival probability of antiparallel and parallel overlaps, showing the probability that an overlap formed by two dynamic MT extensions persists at a given time after its formation (STAR Methods). Semitransparent regions indicate 95% lower and upper confidence bounds.

(D) Quantification of the density of Ase1-mNeonGreen on isolated MTs and (anti)parallel bundles (STAR Methods). The numbers below the boxes denote the number of analyzed MT bundles, ***$p < 0.001$ (Tukey's test).

Panels show data for MT plus ends (minus ends generally were not analyzed).

See also Figure S1 and Video S1.

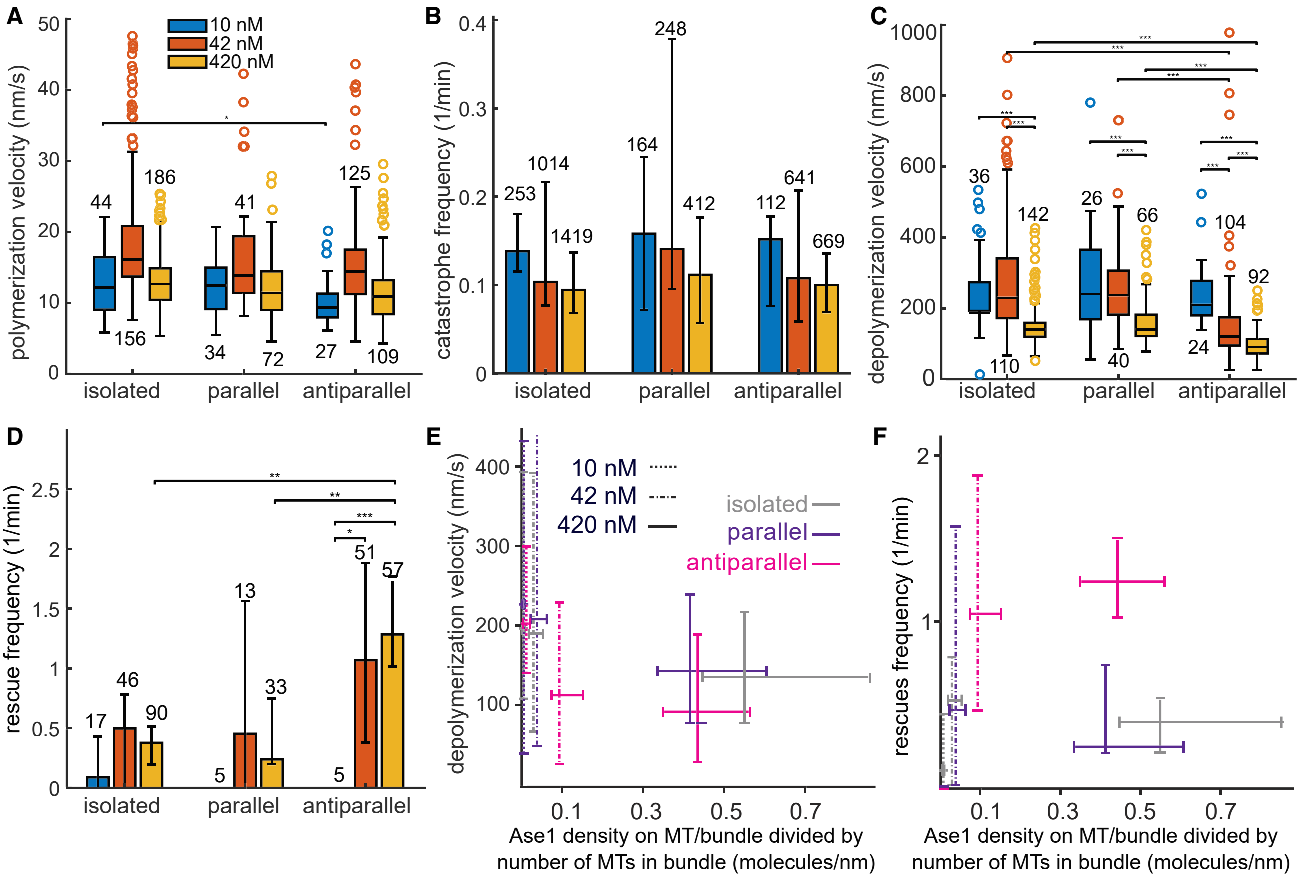

Figure 2. Ase1 differentially regulates the dynamics of microtubules in parallel and antiparallel overlaps

(A–D) Polymerization velocity (A), catastrophe frequency (B), depolymerization velocity (C), and rescue frequency (D) of dynamic MT plus ends in different configurations and in the presence of varying concentrations of Ase1-mNeonGreen.

(E) Depolymerization velocity (see A) versus Ase1-mNeonGreen density on a given MT or bundle divided by number of MTs in that bundle (i.e., the density as shown in Figure 1D is divided by 2 in the case of parallel and antiparallel MTs).

(F) Rescue frequency (see D) versus Ase1-mNeonGreen density (see Figure 1D).

All plots show results for the same experiments as shown in Figure 1. $^*p < 0.05$, $^{**}p < 0.01$, $^{***}p < 0.001$ (Tukey's test). Boxplots are weighted by the length of a sampled period of polymerization or depolymerization. In boxplots, the numbers indicate the number of recorded events; in bar plots, the numbers indicate the sum of the length of all sampled periods of polymerization or depolymerization (in minutes). In bar plots, the height of the bar indicates the catastrophe/rescue frequency as determined from all timelapses (number of total events divided by total duration of depolymerization), while the error bars indicate the lowest and highest rates as determined from each isolated timelapse; velocities are normalized to the median velocity of isolated MTs (STAR Methods).

See also Figure S2.

Stabilization of terminal tubulin subunits by Ase1 is sufficient to reproduce Ase1 sweeping and reduced MT depolymerization velocity

To mathematically analyze the molecular mechanism that causes Ase1 to accumulate at depolymerizing MT ends while reducing their depolymerization velocity, we developed a simple model for an isolated MT. This model treats the MT as a 1D lattice of repeating Ase1 binding sites representing tubulin heterodimers of one MT protofilament and neglects its 3D nature and protofilament structure (STAR Methods). Ase1 binding, unbinding, and hopping to adjacent lattice sites are represented as stochastic events. The associated rates, k_{on} , k_{off}, k_h (Figure 4A), are determined experimentally (Table S1). Only one Ase1 molecule can be attached to any one tubulin heterodimer, meaning that Ase1 can hop only to unoccupied neighboring sites. When reaching the end of an MT, Ase1 can either hop away from this end (if the proximal binding site is unoccupied) or unbind with rate k_{off}, as modeled previously.[20] MT depolymerization is modeled discretely with stochastic detachment of the terminal heterodimer. The rate of depolymerization is affected by Ase1 (Figure 4B). Specifically, this rate is k_d^0 when the terminal tubulin is free of Ase1 and $k_d = (1 - \Omega)k_d^0$ otherwise. The value of k_d^0 is calibrated from the MT depolymerization velocity in the absence of Ase1, measured experimentally (Table S1). The parameter $\Omega \in [0, 1]$ specifies the effect of Ase1 on depolymerization. If $\Omega = 0$, Ase1 has no effect, while if $\Omega = 1$, the terminal subunit cannot unbind while Ase1 is bound. For $\Omega > 0$, this model leads to an accumulation of Ase1 near the depolymerizing end accompanied by a decrease of the depolymerization velocity (Figures 4C–4E, S4A, and S4B). The accumulation occurs because subunits without Ase1 are more likely to be lost at the plus end. Selective loss of tubulin without Ase1 thus increases

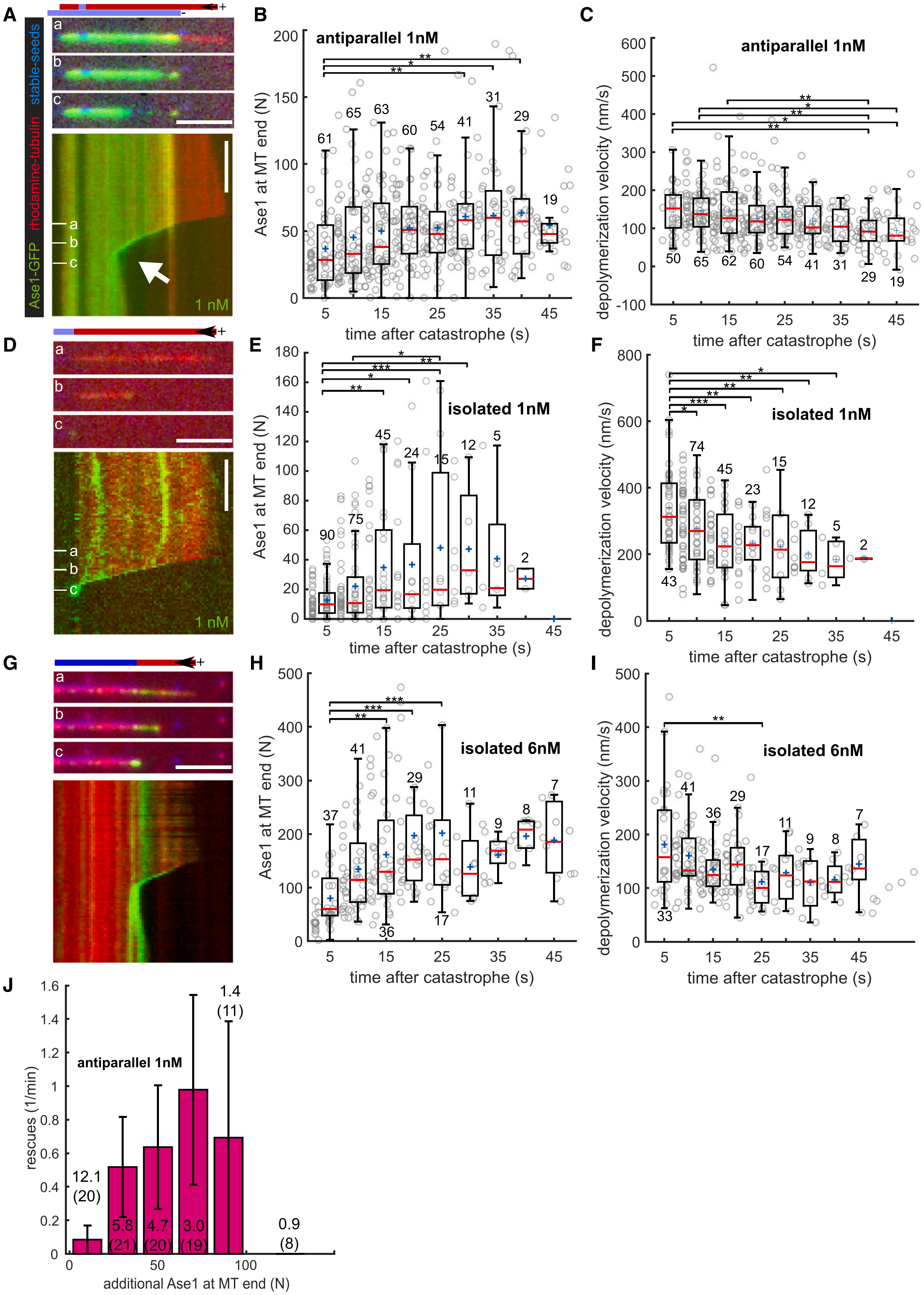

Figure 3. Slower MT depolymerization coincides with accumulation of Ase1 at depolymerizing MT

(A, D, and G) Kymographs of the plus end of depolymerizing MTs in the presence of Ase1-GFP in solution. The stabilized GMPCPP-MT seeds were labeled with 15% rhodamine and 15% Alexa 647 (or, alternatively, with 2% Alexa 647), while the free tubulin in solution was labeled with 7% rhodamine. In sketches, dynamic

(legend continued on next page)

the density of Ase1 at the depolymerizing end, creating a positive feedback that counteracts MT depolymerization. At steady state, the system can be characterized by the probability P_1 of the terminal site to be occupied and the rate of subunit loss, which is $k_d = k_d^0(1 - \Omega P_1)$. This model is sufficient to highlight the fundamental consequences of stabilizing the terminal tubulin subunits but did not fully match the experimental data. We thus generalized this model, assuming that the rate of loss of terminal tubulin subunits is reduced by the same factor $(1 - \Omega)$ if an Ase1 molecule is present in either of the N-terminal sites. Thus, this rate is $k_d = k_0^d\left[1 - \Omega\left\{1 - \prod_{i=1}^{i=N}(1 - P_i)\right\}\right]$, where P_i is the probability of site i being occupied by Ase1. Model parameters were set from experimental measurements except for Ω and N (Table S1). Models with large values of N are unlikely, since they would require Ase1 to influence the detachment of a distant tubulin subunit. We considered the previous model, model 1 ($N = 1$), where only Ase1 bound to the terminal subunits affects its unbinding, and model 2 ($N = 3$), where unbinding is also affected by the 3 terminal subunits. For these two models, we systematically varied Ω and compared the model results with the experimental data. Specifically, we aimed to reproduce the timescale of accumulation of Ase1 and the total amount of Ase1 accumulated and depolymerizing velocity reached at steady state (Table S2). We got the best match with model 2 and $\Omega = 0.9$ (Figures S4A and S4B), which could reproduce the extent and timescale of Ase1 accumulation as well as the steady-state depolymerization velocity for isolated MTs at 6 nM Ase1 (Figures 4C and S4A). With the same parameters, we could recapitulate the Ase1 accumulation timescale and steady-state accumulation for isolated MTs at 1 nM Ase1 (Figures 4D and S4B). In the case of overlaps at 1 nM of Ase1, both models predict a lower number of swept Ase1 molecules than we had measured experimentally but correctly predict that Ase1 molecules have a bigger impact on MT depolymerization in the case of overlaps (Figures S4A–S4C). In summary, built on a simple assumption of how Ase1 would affect the tubulin unbinding rate, this model explains the Ase1 sweeping at shrinking MT ends associated with the slowdown of MT disassembly and recapitulates quantitatively the behavior of the isolated MTs at 6 nM Ase1, and within an order of magnitude for 1 nM Ase1.

In this work, we show that Ase1 selectively stabilizes antiparallel overlaps without substantially affecting the dynamics of isolated MTs or MTs in parallel overlaps. In mitotic spindles and other bipolar MT arrays, this can lead to selective stabilization of the array's central regions, while keeping the rest of the array dynamic and pliable. We observed Ase1 sweeping, the accumulation of lattice-bound, diffusible Ase1 at depolymerizing MT ends, termed "protein sweeping" or "herding," which is analogous to the *in vitro* behavior of the MT-severing enzyme spastin and the kinetochore-associated Ndc80 and Dam1 complexes.[21–27] Like Ase1, Dam1 and Ndc80 complexes accumulate at depolymerizing MT ends and decrease depolymerization velocity.

We produced simple models based on the assumption that Ase1 reduces the detachment of terminal tubulin subunits when bound at the MT tip. This assumption, when allowing for diffusion of Ase1 molecules along the protofilament, leads to both a decrease of MT depolymerization velocity and accumulation of Ase1 at the tip of shrinking MTs. Sweeping occurs because subunits without Ase1 are more likely to be lost at the plus end, and their loss increases the density of Ase1 at the depolymerizing end. Our model quantitatively recapitulated the behavior of the system for 6 nM Ase1 (Figure 4C), and within an order of magnitude for 1 nM Ase1 (Figure 4D). Given the low density of Ase1 molecules at 1 nM concentration (<1% of tubulin dimers bound to Ase1), the discrepancy may be due to stochasticity of the system. Our model did not include MT rescues; however, if one assumes that each crosslink reached by a depolymerizing MT tip has a chance of inducing rescue, as proposed by Stoppin-Mellet et al.,[12] we expect a positive correlation between Ase1 density and rescue frequency, consistent with our experimental data. The quantitative disagreement with experimental data for antiparallelly crosslinked MTs might be due to the fact that Ase1 is not distributed evenly between the protofilaments of a crosslinked MT, with protofilaments involved in crosslinking containing higher densities of Ase1 (Figure 1D). A more complex model accounting for protofilament interactions would be needed for overlaps, informed by experimental measurements of such interactions. Finally, Ase1 is known to display multimerization within antiparallel MT overlaps,[28] which, as reported recently, is an important factor involved in slowdown of motor-driven MT sliding.[29] Multimerization, especially when promoted by the herding of Ase1 molecules at depolymerizing MT tips, might add another layer of complexity to the Ase1-mediated regulation of MT dynamics, possibly resulting in the addition of nonlinearities to the otherwise linear relationship between catastrophe frequency and tubulin concentration.[30] Conversely, herding of the Ase1 crosslinkers might be involved in the slowdown of MT sliding propelled by molecular motors, if the protein traffic jam at the MT tip increases the friction that motors must overcome. Though the cases of MT depolymerization and MT sliding are different in that MT depolymerization does not involve MT movement

extensions with GDP lattices are colored red and stabilized GMPCPP seeds are colored blue or light blue (in case of the weakly labeled seeds). Scale bars, 5 μm and 1 min; contrast and balance vary from panel to panel (each kymograph shows a different MT). White arrows highlight rescue events.

(B, E, and H) The number of additional Ase1 molecules at the end of depolymerizing MTs, plotted over the time passed since the catastrophe. Each data point represents data extracted from one line scan.

(C, F, and I) The frame-to-frame depolymerization velocity of MTs over time (analogous to B, E, and H). Because the exact time of catastrophe is unknown due to limits in temporal resolution, the velocity measurement right after catastrophe underestimates the actual velocity.

(J) Rescue frequency plotted over number of additional Ase1 molecules at the MT end. The duration depolymerized at a respective x value was added to the respective bin. The number of rescues observed in the same bin (N) was then divided by the sum of depolymerization durations (shown in min; the number in parentheses refers to the number of MTs) to estimate the rescue frequency. The correlation coefficient (weighted[19] by sums of depolymerization durations) is 0.67. For an example event, see (A). $^*p < 0.05$, $^{**}p < 0.01$, $^{***}p < 0.001$ (Tukey's test).

See also Figure S3 and Videos S2 and S3.

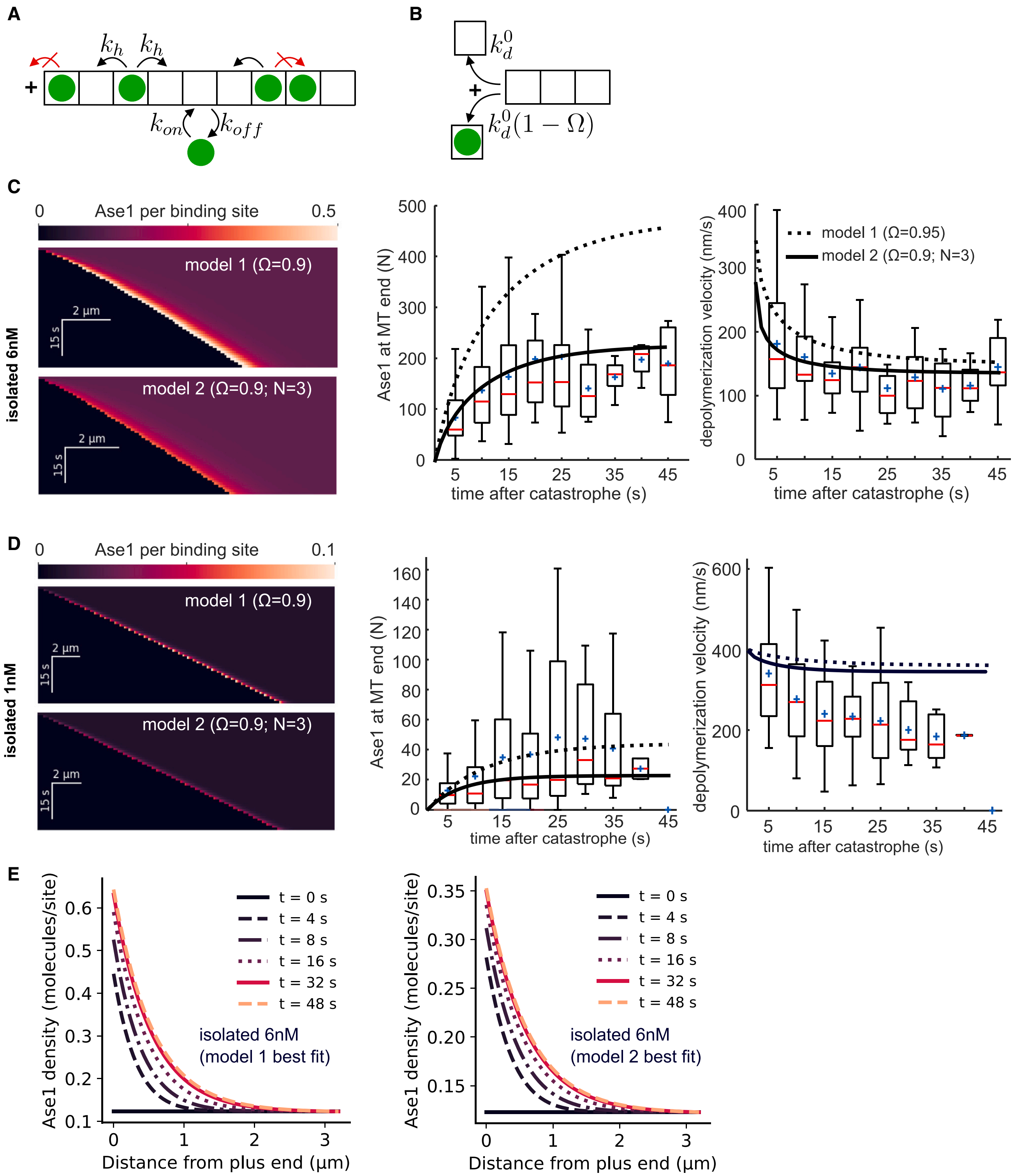

Figure 4. Stabilization of terminal tubulin subunits by Ase1 is sufficient to reproduce Ase1 sweeping and reduced MT depolymerization velocity

(A and B) Cartoons representing model assumptions (STAR Methods).

(A) Ase1 binding, unbinding, and hopping to neighboring sites are stochastic events with constant rates, k_{on} ,k_{off},k_h. Only one Ase1 molecule can be attached to any one tubulin heterodimer, so moving or binding to an occupied binding site is not allowed (red crossed arrow on the right). Ase1 does not fall off from the MT by hopping at its plus ends (red crossed arrow on the left).

(legend continued on next page)

and thus no movement of Ase1 binding sites, herding-driven Ase1 multimerization appears plausible by locally increasing Ase1 density. The possibility of Ase1 molecules acting cooperatively to promote rescues for antiparallel MTs specifically is intriguing and would offer the cell a lever for modulating the rescue-promoting effect of MT crosslinking. A combination of these factors could explain the stronger stabilizing effect of Ase1 on antiparallel overlaps.

Our results show that the presence of diffusible MT crosslinkers is sufficient to establish enduring antiparallel MT overlaps, such as those found in the midzone of mitotic spindles. In such context, Ase1 can work cooperatively with other MT rescue factors such as CLASP[14] or provide an alternative mechanism for selective lifetime enhancement of antiparallel overlaps. We speculate that the impact of diffusible crosslinkers on MT dynamics may be tunable by posttranslational modifications of either the crosslinkers or the MT surface. Such a tunability has recently been proposed for a seemingly related capacity of Ase1, namely the braking of MT sliding caused by molecular motors.[31,32] For actin filament overlaps, it has been observed that F-actin crosslinkers slow down actin depolymerization,[33,34] suggesting that crosslinker-dependent stabilization of filaments may be a fundamental mechanism in cytoskeletal systems.

STAR★METHODS

Detailed methods are provided in the online version of this paper and include the following:

- KEY RESOURCES TABLE
- RESOURCE AVAILABILITY
    - Lead contact
    - Materials availability
    - Data and code availability
- EXPERIMENTAL MODEL AND STUDY PARTICIPANT DETAILS
- METHOD DETAILS
    - Ase1 expression and purification
    - Microtubule seeds assembly
    - Experimental chamber preparation
    - Assay buffer
    - Imaging
    - Image analysis
    - Mathematical modelling
    - Modelling of overlaps
- QUANTIFICATION AND STATISTICAL ANALYSIS
    - Data representation
    - Comparison of experimental data and model

SUPPLEMENTAL INFORMATION

Supplemental information can be found online at https://doi.org/10.1016/j.cub.2024.07.055.

ACKNOWLEDGMENTS

We thank Veronika Vanova and Tereza Smidova for technical support. We acknowledge projects nos. 19-27477X (Z.L.), 22-11753S (M.B.), and 19-17398S (S.H.) from the Czech Science Foundation; project no. 116120 (J.K.) from the Grant Agency of Charles University; the institutional support of the Czech Academy of Sciences (RVO: 86652036); project LX22NPO5107 (MEYS) financed by European Union – Next Generation EU; CMS-Biocev (biophysical techniques) supported by MEYS CR (LM2015043); and the Centre of Imaging Methods core facility, Faculty of Science, Charles University, supported by the Czech-BioImaging through MEYS CR (LM2015062 and CZ.02.1.01/0.0/0.0/16_013/0001775). P.N. and X.L. acknowledge the financial support of 52150710541 from NSFC, P.R. China.

AUTHOR CONTRIBUTIONS

Conceptualization, S.D., M.B., and Z.L.; methodology, J.K., M.L.-R., F.N., S.D., M.B., and Z.L.; investigation, J.K. and M.L.-R.; formal analysis, J.K. and M.L.-R.; data curation, J.K.; validation, J.K.; resources, S.H., L.G., X.L., and P.N.; writing, J.K., M.L.-R., F.N., S.D., M.B., and Z.L.; visualization, J.K. and M.L.-R.; supervision, P.N., F.N., M.B., and Z.L.; funding acquisition, J.K., P.N., M.B., and Z.L.

DECLARATION OF INTERESTS

The authors declare no competing interests.

Received: August 5, 2022
Revised: April 30, 2024
Accepted: July 15, 2024
Published: August 12, 2024

REFERENCES

1. Kirschner, M., and Mitchison, T. (1986). Beyond self-assembly: from microtubules to morphogenesis. Cell *45*, 329–342. https://doi.org/10.1016/0092-8674(86)90318-1.
2. Nédélec, F., Surrey, T., and Karsenti, E. (2003). Self-organisation and forces in the microtubule cytoskeleton. Curr. Opin. Cell Biol. *15*, 118–124. https://doi.org/10.1016/S0955-0674(02)00014-5.
3. Mastronarde, D.N., McDonald, K.L., Ding, R., and McIntosh, J.R. (1993). Interpolar spindle microtubules in PTK cells. J. Cell Biol. *123*, 1475–1489. https://doi.org/10.1083/jcb.123.6.1475.
4. Löiodice, I. (2005). Ase1p organizes antiparallel microtubule arrays during interphase and mitosis in fission yeast. Mol. Biol. Cell *16*, 1756–1768. https://doi.org/10.1091/mbc.E04–10–0899.
5. Yamashita, A., Sato, M., Fujita, A., Yamamoto, M., and Toda, T. (2005). The roles of fission yeast Ase1 in mitotic cell division, meiotic nuclear oscillation, and cytokinesis checkpoint signaling. Mol. Biol. Cell *16*, 1378–1395. https://doi.org/10.1091/mbc.E04-10-0859.
6. Janson, M.E., Loughlin, R., Loïodice, I., Fu, C., Brunner, D., Nédélec, F.J., and Tran, P.T. (2007). Crosslinkers and motors organize dynamic microtubules to form stable bipolar arrays in fission yeast. Cell *128*, 357–368. https://doi.org/10.1016/j.cell.2006.12.030.

(B) In model 1, we assume that the detachment rate of the tubulin terminal subunit is k_d^0 when the first tubulin subunit is free of Ase1 and $k_d = (1 - \Omega)k_d^0$ if Ase1 is bound at the terminal site (for model 2, see main text and STAR Methods).

(C and D) Modeling results for models 1 and 2 with $N = 3$ (experimental data presented in the form of boxplots), for isolated MTs at 6 (C) and 1 nM (D). Left panels: distribution of Ase1 density in time represented as a simulated kymograph (see scale bars). Middle and right panels: values of depolymerization velocity and Ase1 accumulation at steady state derived from experiments (boxplots) or predicted by models 1 and 2 (lines). The boxplots are the same as in the corresponding plots in Figure 3.

(E) Distribution of Ase1 density on terminal sites in time for the indicated time points (see legend) as predicted by models 1 (A) and 2 (B) with model parameters as in (C).

See also Figure S4 and Tables S1 and S2.

7. Bieling, P., Telley, I.a., and Surrey, T. (2010). A minimal midzone protein module controls formation and length of antiparallel microtubule overlaps. Cell *142*, 420–432. https://doi.org/10.1016/j.cell.2010.06.033.
8. She, Z.Y., Wei, Y.L., Lin, Y., Li, Y.L., and Lu, M.H. (2019). Mechanisms of the Ase1/PRC1/MAP65 family in central spindle assembly. Biol. Rev. *94*, 2033–2048. https://doi.org/10.1111/brv.12547.
9. Subramanian, R., Wilson-Kubalek, E.M., Arthur, C.P., Bick, M.J., Campbell, E.A., Darst, S.A., Milligan, R.A., and Kapoor, T.M. (2010). Insights into antiparallel microtubule crosslinking by PRC1, a conserved nonmotor microtubule binding protein. Cell *142*, 433–443. https://doi.org/10.1016/j.cell.2010.07.012.
10. Kellogg, E.H., Howes, S., Ti, S.C., Ramírez-Aportela, E., Kapoor, T.M., Chacón, P., and Nogales, E. (2016). Near-atomic cryo-EM structure of PRC1 bound to the microtubule. Proc. Natl. Acad. Sci. USA *113*, 9430–9439. https://doi.org/10.1073/pnas.1609903113.
11. Gaillard, J., Neumann, E., Van Damme, D., Stoppin-Mellet, V., Ebel, C., Barbier, E., Geelen, D., and Vantard, M. (2008). Two microtubule-associated proteins of Arabidopsis MAP65s promote antiparallel microtubule bundling. Mol. Biol. Cell *19*, 4534–4544. https://doi.org/10.1091/mbc.e08-04-0341.
12. Stoppin-Mellet, V., Fache, V., Portran, D., Martiel, J.L., and Vantard, M. (2013). MAP65 coordinate microtubule growth during bundle formation. PLoS One *8*, e56808. https://doi.org/10.1371/journal.pone.0056808.
13. Mani, N., Wijeratne, S.S., and Subramanian, R. (2021). Micron-scale geometrical features of microtubules as regulators of microtubule organization. eLife *10*, e63880. https://doi.org/10.7554/eLife.63880.
14. Bratman, S.V., and Chang, F. (2007). Stabilization of overlapping microtubules by fission yeast CLASP. Dev. Cell *13*, 812–827. https://doi.org/10.1016/j.devcel.2007.10.015.
15. Liu, J., Wang, Z., Jiang, K., Zhang, L., Zhao, L., Hua, S., Yan, F., Yang, Y., Wang, D., Fu, C., et al. (2009). PRC1 cooperates with CLASP1 to organize central spindle plasticity in mitosis. J. Biol. Chem. *284*, 23059–23071. https://doi.org/10.1074/jbc.M109.009670.
16. Kitazawa, D., Matsuo, T., Kaizuka, K., Miyauchi, C., Hayashi, D., and Inoue, Y.H. (2014). Orbit/CLASP is required for myosin accumulation at the cleavage furrow in Drosophila male meiosis. PLoS One *9*, e93669. https://doi.org/10.1371/journal.pone.0093669.
17. Luchniak, A., Kuo, Y.W., McGuinness, C., Sutradhar, S., Orbach, R., Mahamdeh, M., and Howard, J. (2023). Dynamic microtubules slow down during their shrinkage phase. Biophys. J. *122*, 616–623. https://doi.org/10.1016/j.bpj.2023.01.020.
18. Drechsler, H., Xu, Y., Geyer, V.F., Zhang, Y., and Diez, S. (2019). Multivalent electrostatic microtubule interactions of synthetic peptides are sufficient to mimic advanced MAP-like behavior. Mol. Biol. Cell *30*, 2953–2968. https://doi.org/10.1091/mbc.E19-05-0247.
19. Pelletier, G. (2024). Weighted correlation and covariance (weightedcorrs). https://github.com/gjpelletier/weightedcorrs.
20. Braun, M., Lansky, Z., Fink, G., Ruhnow, F., Diez, S., and Janson, M.E. (2011). Adaptive braking by Ase1 prevents overlapping microtubules from sliding completely apart. Nat. Cell Biol. *13*, 1259–1264. https://doi.org/10.1038/ncb2323.
21. Powers, A.F., Franck, A.D., Gestaut, D.R., Cooper, J., Gracyzk, B., Wei, R.R., Wordeman, L., Davis, T.N., and Asbury, C.L. (2009). The Ndc80 kinetochore complex forms load-bearing attachments to dynamic microtubule tips via biased diffusion. Cell *136*, 865–875. https://doi.org/10.1016/j.cell.2008.12.045.
22. Grishchuk, E.L., Efremov, A.K., Volkov, V.A., Spiridonov, I.S., Gudimchuk, N., Westermann, S., Drubin, D., Barnes, G., McIntosh, J.R., and Ataullakhanov, F.I. (2008). The Dam1 ring binds microtubules strongly enough to be a processive as well as energy-efficient coupler for chromosome motion. Proc. Natl. Acad. Sci. USA *105*, 15423–15428. https://doi.org/10.1073/pnas.0807859105.
23. Al-Hiyasat, A., Tuna, Y., Kuo, Y., and Howard, J. (2023). Herding of proteins by the ends of shrinking polymers. Phys. Rev. E *107*, L042601. https://doi.org/10.1103/PhysRevE.107.L042601.
24. Lombillo, V.A., Stewart, R.J., and Richard McIntosh, J. (1995). Minus-end-directed motion of kinesin–coated microspheres driven by microtubule depolymerization. Nature *373*, 161–164. https://doi.org/10.1038/373161a0.
25. Franck, A.D., Powers, A.F., Gestaut, D.R., Gonen, T., Davis, T.N., and Asbury, C.L. (2007). Tension applied through the Dam1 complex promotes microtubule elongation providing a direct mechanism for length control in mitosis. Nat. Cell Biol. *9*, 832–837. https://doi.org/10.1038/ncb1609.
26. Umbreit, N.T., Gestaut, D.R., Tien, J.F., Vollmar, B.S., Gonen, T., Asbury, C.L., and Davis, T.N. (2012). The Ndc80 kinetochore complex directly modulates microtubule dynamics. Proc. Natl. Acad. Sci. USA *109*, 16113–16118. https://doi.org/10.1073/pnas.1209615109.
27. Grishchuk, E.L. (2017). Biophysics of microtubule end coupling at the kinetochore. Prog. Mol. Subcell. Biol. *56*, 397–428. https://doi.org/10.1007/978-3-319-58592-5_17.
28. Kapitein, L.C., Janson, M.E., van den Wildenberg, S.M.J.L., Hoogenraad, C.C., Schmidt, C.F., and Peterman, E.J.G. (2008). Microtubule-driven multimerization recruits ase1p onto overlapping microtubules. Curr. Biol. *18*, 1713–1717. https://doi.org/10.1016/j.cub.2008.09.046.
29. Alfieri, A., Gaska, I., and Forth, S. (2021). Two modes of PRC1-mediated mechanical resistance to kinesin-driven microtubule network disruption. Curr. Biol. *31*, 2495–2506.e4. https://doi.org/10.1016/j.cub.2021.03.034.
30. Walker, R.A., O'Brien, E.T., Pryer, N.K., Soboeiro, M.F., Voter, W.A., Erickson, H.P., and Salmon, E.D. (1988). Dynamic instability of individual microtubules analyzed by video light microscopy: rate constants and transition frequencies. J. Cell Biol. *107*, 1437–1448. https://doi.org/10.1083/jcb.107.4.1437.
31. Fu, C., Ward, J.J., Loiodice, I., Velve-Casquillas, G., Nedelec, F.J., and Tran, P.T. (2009). Phospho-regulated interaction between kinesin-6 Klp9p and microtubule bundler Ase1p promotes spindle elongation. Dev. Cell *17*, 257–267. https://doi.org/10.1016/j.devcel.2009.06.012.
32. Thomas, E.C., Ismael, A., and Moore, J.K. (2020). Ase1 domains dynamically slow anaphase spindle elongation and recruit Bim1 to the midzone. Mol. Biol. Cell *31*, 2733–2747. https://doi.org/10.1091/mbc.E20-07-0493-T.
33. Schmoller, K.M., Semmrich, C., and Bausch, A.R. (2011). Slow down of actin depolymerization by cross-linking molecules. J. Struct. Biol. *173*, 350–357. https://doi.org/10.1016/j.jsb.2010.09.003.
34. Maul, R.S., Song, Y., Amann, K.J., Gerbin, S.C., Pollard, T.D., and Chang, D.D. (2003). EPLIN regulates actin dynamics by cross-linking and stabilizing filaments. J. Cell Biol. *160*, 399–407. https://doi.org/10.1083/jcb.200212057.
35. Schindelin, J., Arganda-Carreras, I., Frise, E., Kaynig, V., Longair, M., Pietzsch, T., Preibisch, S., Rueden, C., Saalfeld, S., Schmid, B., et al. (2012). Fiji: an open-source platform for biological-image analysis. Nat. Methods *9*, 676–682. https://doi.org/10.1038/nmeth.2019.
36. Castoldi, M., and Popov, A.V. (2003). Purification of brain tubulin through two cycles of polymerization- depolymerization in a high-molarity buffer. Protein Expr. Purif. *32*, 83–88. https://doi.org/10.1016/S1046-5928(03)00218-3.
37. Gell, C., Friel, C.T., Borgonovo, B., Drechsel, D.N., Hyman, A., and Howard, J. (2011). Purification of tubulin from porcine brain. Methods Mol. Biol. *777*, 15–28. https://doi.org/10.1007/978-1-61779-252-6.
38. Zhang, H., Pekárek, J., Feng, J., Liu, X., Li, H., Zhu, H., Svatoš, V., Gablech, I., Podešva, P., Ni, S., et al. (2020). Simplifying the design complexity of microfluidic chips. J. Vac. Sci. Technol. B *38*, 063002. https://doi.org/10.1116/6.0000562.
39. Coimbatore Balram, K., Westly, D.A., Davanco, M.I., Grutter, K.E., Li, Q., Michels, T., Ray, C.H., Kasica, R.J., Wallin, C.B., Gilbert, I.J., et al.

(2016). The nanolithography toolbox. J. Res. Natl. Inst. Stand. Technol. *121*, 464–475. https://doi.org/10.6028/jres.121.024.

40. Castro, E.R., Tarn, M.D., Ginterová, P., Zhu, H., Xu, Y., and Neužil, P. (2018). Determination of dynamic contact angles within microfluidic devices. Microfluid. Nanofluidics *22*, 51. https://doi.org/10.1007/s10404-018-2066-0.
41. Mahamdeh, M., Simmert, S., Luchniak, A., Schäffer, E., and Howard, J. (2018). Label-free high-speed wide-field imaging of single microtubules using interference reflection microscopy. J. Microsc. *272*, 60–66. https://doi.org/10.1111/jmi.12744.
42. Ruhnow, F., Zwicker, D., and Diez, S. (2011). Tracking single particles and elongated filaments with nanometer precision. Biophys. J. *100*, 2820–2828. https://doi.org/10.1016/j.bpj.2011.04.023.

STAR★METHODS

KEY RESOURCES TABLE

REAGENT or RESOURCE	SOURCE	IDENTIFIER
Antibodies		
Goat Anti-Biotin	Sigma Aldrich	Cat#B3640; RRID: AB_258552
Bacterial and virus strains		
E. coli strain BL21 (DE3)	Altium International	Cat#230280
Chemicals, peptides, and recombinant proteins		
Benzonase	Novagen	Cat#70664
cOmplete Protease inhibitor cocktail EDTA-free	Roche Diagnostics GmBH	Cat#11873580001
HRV 3C protease	Merck Milipore	Cat#71493
Biotin-labeled tubulin	Cytoskeleton	Cat#T333P
GTP	Jena Bioscience	Cat#NU-1012
GMPCPP	Jena Bioscience	Cat#NU-405
Dichlorodimethylsilane (DDS)	Sigma Aldrich	Cat#440272
Pluronic F127	Sigma Aldrich	Cat#P2443
Methylcellulose	Sigma Aldrich	Cat#M0512
Recombinant DNA		
Ase1-GFP-6xHis, pET28 backbone	Janson et al.[6]	N/A
Ase1-mNeonGreen-6xHis, pET11 backbone	this manuscript	N/A
Software and algorithms		
Modelling code and code for recreating Figure 4	this manuscript	Zenodo: https://doi.org/10.5281/zenodo.12169420
Poetry (python dependency manager)	github.com/python-poetry	https://python-poetry.org/
Python	Python Software Foundation	https://www.python.org/; RRID: SCR_008394
Code for creating kymographs	this authorgroup	Zenodo: https://doi.org/10.5281/zenodo.3270572
Code for analyzing kymographs and recreating Figures 1, 2, and 3	this manuscript	Zenodo: https://doi.org/10.5281/zenodo.12517251
MATLAB (R2019a)	MathWorks	https://www.mathworks.com/products/matlab.html; RRID: SCR_001622
ImageJ 1.52 (FIJI)	Schindelin et al.[35]	https://imagej.nih.gov/ij/; RRID SCR_002285
Other		
Amicon Ultra-15	Merck	Cat#UFC910024

RESOURCE AVAILABILITY

Lead contact

Further information and requests for resources and reagents should be directed to and will be fulfilled by the lead contact, Zdenek Lansky (Zdenek.Lansky@ibt.cas.cz).

Materials availability

The plasmid Ase1-mNeonGreen-6xHis (pET11 backbone) is available from the lead contact upon request.

Data and code availability

- All original code used to generate and analyze the theoretical model simulations has been deposited at Zenodo and is publicly available as of the date of publication (Zenodo: https://doi.org/10.5281/zenodo.12169420). The DOI is listed in the key resources table (modelling code). The simulation data generated with the code as well as the experimental data used to compare with the theoretical results are deposited in the same Zenodo entry. To ensure reproducibility of the computational environment, the python library dependencies were managed using poetry (see key resources table).
- All original code used for analyzing kymographs (see "estimation of amount of Ase1 being swept" in method details) and recreating Figures 1, 2, and 3 has been deposited at Zenodo (Zenodo: https://doi.org/10.5281/zenodo.12517251). Tabular data

from which graphs in Figures 1, 2, 3, and S1–S3 can be recreated are also available there. Any additional information required to reanalyze the data reported in this paper is available from the lead contact upon request.

EXPERIMENTAL MODEL AND STUDY PARTICIPANT DETAILS

Ase1-GFP and Ase1-mNeonGreen were expressed in e.coli cells (Altium International, #230280).

METHOD DETAILS

Ase1 expression and purification

Ase1-GFP[6] and Ase1-mNeonGreen were expressed in E. coli strain BL21 (DE3) (Altium International, #230280). After harvesting the cells, the cell pellet was resuspended in 5 mL ice-cold phosphate buffered saline (PBS) and stored at - 80°C for further use. For cell lysis, the cells were homogenized in 30 mL ice-cold His-Trap buffer (50 mM Na-phosphate buffer, pH 7.5, 5% glycerol, 300 mM KCl, 1 mM MgCl2, 0.1% tween 20, 10 mM BME, 0.1 mM ATP) supplemented with 30 mM imidazole, Protease Inhibitor Cocktail (cOmplete, EDTA free, Roche, #11873580001) and benzonase (Novagen, #70664) to the final concentration of 25 units/mL, then sonicated, and finally centrifuged at 45000 x g for 60 min at 4°C in the Avanti J-26S ultracentrifuge (JA-30.50Ti rotor, Beckman Coulter). The cleared cell lysate was incubated in a lysis buffer-equilibrated Ni-NTA resin (HisPur Ni-NTA Superflow Agarose, Thermo Scientific) for 2 h at 4°C. The Ni-NTA resin was sequentially washed with wash buffer I (His-Trap buffer supplemented with 60 mM imidazole), and wash buffer II (His-Trap buffer supplemented with 60 mM imidazole and 700 mM NaCl). Ase1-GFP was eluted in His-Trap buffer supplemented with 300 mM imidazole. For Ase1-mNeonGreen, after wash buffer II, the resin was washed again in wash buffer I, now supplemented with the 3C PreScisson protease (Merck Milipore, #71493), which cut Ase1-mNeonGreen off the column, at the 3C protease cleavage site positioned in between the mNeonGreen and the 6xHis-tag. The mixture was incubated over night at 4°C. Next day the beads were removed and the cleaved protein was collected. Ase1-GFP and Ase1-mNeonGreen were concentrated by spinning the sample at 3500 RPM at 4°C using a 100kDa centrifugal filter tube (Amicon Ultra-15, Merck, #UFC910024). The second purification step for Ase1-mNeonGreen involved size exclusion chromatography, performed using a Superdex 200 10/300 column. The size exclusion buffer consisted of 100 mM Tris, 150 mM NaCl, 1 mM $MgCl_2$, 1 mM DTT, 0.05% Tween, 0.1 mM ATP, and 10% glycerol. Fractions containing the protein were collected, concentrated, The final protein concentrations were measured with a NanoDrop ND-1000 spectrophotometer (Thermo Scientific) at both 280 and 506 nm absorbance. Protein was flash-frozen in liquid nitrogen and stored at −80°C. All steps in the purification were performed at 4°C.

Microtubule seeds assembly

Porcine brains were obtained from a local abattoir and used within approx. 4 h of death. Porcine brain tubulin was isolated using the high-molarity PIPES procedure.[36,37] Biotin-labeled tubulin was purchased from Cytoskeleton Inc. (#T333P). GMPCPP-microtubule seeds were polymerized from 4 mg/mL tubulin (labelled depending on assay, as described in “experimental chamber preparation”) for 2 h at 37°C in BRB80 supplemented with 1mM MgCl2 and 1mM GMPCPP (#NU-405, Jena Bioscience). The polymerized MTs were centrifuged for 30 min at 18000 x g in a Microfuge 18 Centrifuge (Beckman Coulter). After centrifugation, the pellet with MTs was resuspended, kept in BRB80 at room temperature and used within one week.

Experimental chamber preparation

For TIRF experiments, chambers were assembled by melting thin strips of parafilm in between two glass coverslips silanized with 0.05% dichlorodimethylsilane (DDS, #440272, Sigma).[20] Chambers were never re-used for additional experiments. For some experiments, flow chambers were fabricated on silicon-on-insulator substrate with a diameter of ≈100 mm and nominal value of the top silicon layer thickness of 50 μm based on a design prepared in Nanolithography toolbox software.[38,39] Two lithography steps were performed, one defining the flow chamber, the second one for through holes. We etched the top silicon and stopped it at the buried SiO_2 layer with no Si residue there, followed by anodic bonding of the silicon wafer with fabricated chambers and through holes to the corning glass type Corning 7740 with nominal thickness of 170 μm, subsequent dicing by a diamond blade dicing saw into isolated chips and coating with FAS-17 fluorosilane.[40]

Biotin antibodies were flushed into the channels for 1 min (#B3640, Sigma, 20 μg mL^{-1} in PBS). The glass surface was then blocked by incubation with 1% Pluronic (F127 in PBS, #P2443, Sigma) for at least 20 min, followed by wash with TIRF assay buffer (see below). Biotinylated, GMPCPP-stabilized, fluorescence-labeled MTs in BRB80 (80 mM Pipes/KOH pH 6.9, 1 mM $MgCl_2$, 1 mM EGTA) were then flushed into the channel and bound to the biotin antibodies. Subsequently, the buffer in the flow cell was exchanged for assay buffer (see below). Then, Ase1 in assay buffer was flushed into the flow cell at the final assay concentration stated in the main text, together with tubulin. Set A experiments (Figures 1, 2, S1, and S2) were performed at room temperature and with 30μM unlabeled tubulin present in solution. Set B experiments (Figures 3, 4, and S3) were performed at 29°C and with 14μM tubulin, 7% of which was labeled with rhodamine. In the case of set B experiments, non-biotinylated GMPCPP-stabilized MTs were flushed into the flow cell and bound to the template MTs that were sparsely covered sparsely with Ase1 (these steps were performed before the assay buffer had been flushed in). These MTs were labelled with both rhodamine and Alexa 647 (represented in sketches in dark blue), while the templates were only (very weakly) labelled with Alexa 646 (represented in sketches in light blue). To prevent evaporation in order to avoid changes in component concentrations, the channels were sealed after flushing in the assay buffer.

Assay buffer

The following buffer components common to all used buffers: 20mM PIPES pH 6.9, 10mM HEPES pH 7.2, 0.5mM EGTA, 1mM $MgCl_2$, 0.5mM Mg-ATP, 0.67mM GTP (Jena Bioscience, #NU-1012), 0.67% Tween 20, 6.7mM DTT, 0.3 mg/mL Casein, 13.5mM D-Glucose, 0.3 mg/ml glucose oxidase and 0.03 mg/ml catalase. The buffer for set A experiments, in addition to these components, contained 70mM KCl, and 0.1% methylcellulose (Sigma, #M0512), 0.1% glycerol, 1mM sodium phosphate and 1μM ATP. The buffer for set B experiments, in addition to the components common to all buffers, contained 116mM KCl and 0.065% methylcellulose (Sigma, #M0512).

Imaging

Labeled proteins were visualized sequentially by switching between the corresponding channels (Chroma filter-cubes) using Nikon-Ti E microscope equipped with a 100x Nikon TIRF objective in combination with a Hamamatsu Orca Flash 4.0 sCMOS camera (set A experiments) or 63× Zeiss oil immersion TIRF objective in combination with a Andor iXon DV 897 (Andor Technology) EMCCD camera (set B experiments). In the case of set A experiments, at Ase1 concentrations lower than 40nM, interference reflection microscopy (IRM) was used to visualize the MTs (using the same objective and camera).[41] The acquisition rate was 5 s for set A experiments and 2.5 s for set B experiments, the exposure time was 100ms for both cases. For set B experiments, the Alexa 647-labeled MT seeds were imaged before the start of the time lapse, and only the Ase1-mNeonGreen channel was imaged during the time lapse. For set B experiments, the rhodamine (tubulin) and the GFP (Ase1) channel where imaged sequentially, whereas every 40th frame the Alexa 647 channel was imaged in place of the GFP channel, in order to track the location of the GMPCPP-stabilized seeds (which we with this data determined to not move significantly during experiment time).

Image analysis

Data was analyzed using FIJI 1.52[35] and custom-written MATLAB (Mathworks) routines (https://doi.org/10.5281/zenodo.12517251).

Overlap lifetime estimation

The lifetime of regions of MT overlap was estimated for two different configurations: Antiparallel overlaps, where two dynamic extensions met and formed a dynamic "midzone", and parallel bundles of two dynamic extensions (as shown in Figure 1). For both antiparallel and parallel overlaps, lifetime was taken to start upon the bundling of the dynamic (GDP) lattices of each involved MT (for antiparallel configurations, we additionally required both plus ends to be within 3 μm to each other upon start of the event). Lifetime was taken to end upon one of the involved MTs to shrink back to its GMPCPP-stabilized region for parallel bundles, and upon the midzone ceasing to exist for antiparallel bundles. The plot is a Kaplan-Meier plot, which adequately accounts for cases where an overlapping region survived until the end of the recorded time-lapse Video (i.e., cases which were right-censored) (Figure 1C was generated by using the MATLAB function ecdf with setting "survival" and alpha = 0.05).

Estimation of parameters of MT dynamics

Parameters of MT dynamics, for set A experiments, have been estimated by generating kymographs and approximating the location of MT plus ends over time and space with straight lines (the Ase1-mNeonGreen signal was used to visually track MT ends, as MT were not imaged directly). For set B experiments, we used FIESTA to determine the locations of MTs.[42] Both methods yielded polymerization and depolymerization velocities. Rescues were identified as events where a MT switches from depolymerization to polymerization before reaching the GMPCPP-stabilized seed, and catastrophes were events where polymerization was followed by depolymerization. Rescue and catastrophe frequencies were estimated by dividing the number of rescues respectively catastrophes by the sum of the total distance depolymerized respectively polymerized by all plus ends. In the case of set A experiments, we tested the 10nM only during the revision, during a time where room temperatures were less stable. Therefore, MT velocities differed from our initial experiments across all Ase1 concentrations. To be able to pool the results from these experiments with our initial results, we multiplied the velocities of these experiments by the following factor: The mean polymerization respectively depolymerization velocity of isolated MTs at 42nM of the initial experiments divided by the mean respective velocity of isolated MTs at 42nM of the experiments performed during revision (these mean velocities were weighted by the duration of each polymerization/depolymerization event). The resulting factors were 0.4 for polymerization and 0.39 for depolymerization.

Single fluorophore quantification

Fluorescent signal of a single Ase1-mNeonGreen dimer was determined by generating intensity time-traces of Ase1-mNeonGreen molecules and estimating the height of the occurring steps in change of intensity (only small steps, i.e., steps likely to be bleaching steps). The number of steps was first estimated by eye, and this number was used as input for the *findchangepoints* function of MATLAB to determine the position of the steps (by detection of significant changes of the mean value). To yield the intensity per Ase1 dimer, the median of the heights of these steps was calculated and multiplied by two. For the estimation of single Ase1-GFP dimers, the intensity of single diffusive spots of GFP signals on MTs has been taken at very low concentration of Ase1-GFP in the buffer (no bleaching data available for these experiments). For estimation of single fluorophores for set B experiments we did not have bleaching data available, instead we measured the intensity of diffusing molecules (which may overestimate the intensity per single molecule).

Ase1 density estimation

Area selections along the MT length (only regions with at least one dynamic extension present were measured) were used to readout the mEGFP or mCherry fluorescent signal and to estimate the integrated signal intensity of GFP- or mNeonGreen-labeled Ase1 bound to the MT. The signal in regions directly adjacent to the MT was subtracted as background signal. The density of GFP- or mNeonGreen -labeled Ase1 bound to the MT was then estimated by dividing the integrated intensity by the estimated intensity per single fluorescent molecule (either GFP or mNeonGreen, see below) and the length of the region. The signal per length (S) measured on isolated MTs was used to correct for the reduced illumination intensity in outer regions of the field of view, in cases where a region of interest (ROI) was located in such a region ($S_{corrected}$(ROI) = S(ROI) *S(isolated MT in center of field of view) / S(isolated MT near ROI).

Estimation of amount of Ase1 being swept

To estimate the number of swept Ase1 molecules for corresponding panels in Figures 3, 4, and S3 (set B experiments), we first obtained density traces for each frame during a MT depolymerization period. These traces were obtained by summing the pixel intensities perpendicular to the MT, i.e., by generating a kymograph where each pixel represents such a sum (https://doi.org/10.5281/zenodo.3270572). For each frame f we analyzed the corresponding density trace D_f as follows. (1) We computed D_s by subtracting the density trace $D_{before\_catastrophe}$ of the MT before the catastrophe had occurred from D_f ($D_s = D_f - D_{before\_catastrophe}$) (2) We obtained $x = 0 = X_{Dsmax}$, the location of the local maximum of D_s in vicinity of the MT plus end. (3) We obtained $X_{Dsright}$ by finding the first local minimum of D_s to the right of $X_{Dsright}$ (to reduce the effect of noise, we smoothed D_s for this computation). "Right" of D_s, in our chosen coordinate system, means toward the MT seed (x > 0). (4) $X_{Dsleft} = X_{Dsmax} - 471$nm (471 nm = 3 pixels). (5) We computed D_A. D_A is equal to D_f to the left of X_{Dsmax}, and equal to $D_s + D_f(X_{Dsmax}) - D_s(X_{Dsmax})$ to the right of X_{Dsmax}. (6) We fitted a distribution Y_F (shape see below) plus an error function Y_E to D_A between X_{Dsleft} and $X_{Dsright}$. We required both Y_F and the error function to not have any x-offset: Y_F was a right-sided decaying exponential $\exp(-x/\lambda)$ ($Y_F = 0$ where $x < 0$, and with λ bounded between 1 and 1000 nm) convolved with a Gaussian $\exp(-x^2/2\sigma^2)$ (with σ bounded between 180 and 190 nm to account for the point spread function of our setup; this same σ had been used as input for Y_E). We also fixed G + E (plus a constant value) to approach the minimum of D_A to the left of the end, and the average of D_A to the right of $X_{Dsright}$ (the average of D_A within 5 μm from $X_{Dsright,}$ giving more weight to values close to $X_{Dsright}$). (6) We then summed the Ase1 density below Y_F (as discretized in x by the pixel size), which we took as a proxy for the number of swept Ase1-GFP molecules after dividing by the intensity per Ase1 dimer (obtained as described above).

Fluorescence recovery after photo bleaching (FRAP)

Biotinylated GMPCPP-stabilized MTs were immobilized on the coverslip. We then flushed in the same assay buffer as for set A experiments, incubated until the Ase1 density on MTs reached a steady-state, and subsequently bleached Ase1-mNeonGreen molecules and recorded the recovering Ase1-mNeonGreen signal. We fitted the resulting recovery curve to the expression $D_s - c\exp(-bt)$, where D_s is the steady state density, and c and b are fitting parameters. Results for fitting parameter b are shown in Figure S4D.

Mathematical modelling

The scripts to reproduce the modelling, and to plot experimental and theoretical results from Figures 4 and S4 can be found in https://doi.org/10.5281/zenodo.12169420.

Assumptions

The model of Ase1 accumulation on depolymerizing MTs, and its effect on depolymerization velocity (Figure 4A) is built on the following assumptions.

(1) We neglect interactions between protofilaments and only consider a one-dimensional lattice, where lattice of size $a = 8$nm start at index $i = 1$ at the plus end, extending to $i = 400$.
(2) Only bound Ase1 molecules are considered by recording the presence or absence (0 or 1) of Ase1 in each lattice site. Bound Ase1 molecules exchange with solution with two constant rates (k_{on} ,k_{off}). Binding is only allowed if the lattice site is empty (Figure 4A). k_{off} was directly measured, and k_{on} was adjusted to match the Ase1 equilibrium density on MTs (Table S1).
(3) Ase1 particles on the lattice undergo unbiased diffusion characterized by a constant hopping rate (k_h). Hopping is only allowed to an empty site (Figure 4A). The rate k_h is calculated from the experimentally measured diffusion coefficient of Ase1 (Table S1), as $k_h = D/a^2$.
(4) The Ase1 particle in the terminal site ($i = 1$), cannot hop past the MT end (red arrow on the left of Figure 4A), but can detach with rate k_{off}.
(5) The terminal lattice site may dissociate from the MT, with rate k_d which depends on the presence of Ase1, according to each model:
   a. In Model 1, it occurs with rate k_d^0 if the terminal lattice site is not occupied (Figure 4B top), and with rate $(1 - \Omega)k_d^0$ if it is occupied (Figure 4B bottom). Ω is a parameter between zero and one. If $\Omega = 0$, the presence of Ase1 has no effect, and if $\Omega = 1$, the first tubulin subunit cannot unbind if it is bound to Ase1.
   b. In Model 2, the rate of tubulin subunits loss at the plus end is reduced by a factor $(1 - \Omega)$ if any of the N terminal sites is occupied. At steady state, this rate is $k_d = k_0^d\left[1 - \Omega\left\{1 - \prod_{i=1}^{i=N}(1 - P_i)\right\}\right]$, where P_i is the probability of site i being occupied by Ase1.

k_d^0 is derived from the depolymerization rate of MTs in the absence of Ase1 (v_0), measured experimentally (Table S1), such that $k_d^0 = v_0/a$.

(6) If the terminal lattice site dissociates when a molecule of Ase1 is bound to it, this Ase1 is lost as well (Figure 4B, bottom).

Simplification to a system of constant size

Since terminal subunits are more likely to be lost when they are without Ase1 than when they are with Ase1, any dissociation event increases the density of Ase1 remaining on the MT. This effect is only present at the MT end, and away from the end, the probability of a binding site being occupied is only determined by the binding and unbinding constants: $\alpha = k_{on}/(k_{on} + k_{off})$.

Therefore, we can restrict the model to a section of the MT with L lattice sites, as long as the probability of finding a molecule at position L is close to α. When a depolymerisation event happens, we shift the lattice indexes such that site $i+1$ becomes site i, and set $P_{i=L} = \alpha$.

Mean field theory

The system can be solved using a mean-field approximation, by just considering the ensemble of P_i, the average probability of a site i being occupied and neglecting higher-order correlations between neighbouring sites. We can then write a set of discrete differential equations to represent the dynamics of the system:

$$\frac{dP_i}{dt} = (P_{i+1} + P_{i-1} - 2P_i)k_h + (1 - P_i)k_{on} - P_i k_{off} + (P_{i+1} - P_i)k_d$$

Specific equations apply at the boundaries $i = 1$ and L:

$$\frac{dP_1}{dt} = k_h(P_2 - P_1) - P_1 k_{off} + (1 - P_1)k_{on} + k_d P_2 - k_d^0 P_1(1 - \Omega)$$

$$\frac{dP_L}{dt} = 0$$

The terms of the equation are associated with the rates of diffusion, binding, unbinding (k_h, k_{on}, k_{off}) which are constant, and the depolymerization rate (k_d), which is affected by lattice occupancy in a different way in each model (see Assumptions).

For Model 1, $k_d = k_d^0(1 - \Omega P_1)$.

For Model 2, $k_d = k_0^d[1 - \Omega + \Omega\prod_{i=1}^{i=N}(1 - P_i)]$.

This dynamical system can be evolved from any initial conditions, converging to the unique steady-state solution for a set of given parameters. Assuming that the MT is at binding equilibrium when it starts depolymerizing, we initially set $P_i = \alpha$ for all sites. From those initial conditions, we integrate the equations numerically using Python's *odeint* function (see source code).

Modelling of overlaps

To model MT overlaps (Figure 4E), we assume that the Ase1 measured in the overlaps (see Image Analysis above) is evenly distributed among 3 protofilaments that are involved in crosslinking the MTs. We neglect the other protofilaments. We had also modelled 2 protofilaments instead of 3, which did not fit the experimental data as well as 3 protofilaments.

QUANTIFICATION AND STATISTICAL ANALYSIS

All experiments were quantified by pooling data from multiple experiments performed on at least two different days. No data was excluded from the study.

Data representation

In all boxplots presented in the figures, horizontal midline indicates the median; plus symbols indicate the mean; bottom and top box edges indicate the 25th and 75th percentiles, respectively; the whiskers extend to the most extreme data points not considered as outliers (the function *Alternative boxplot* from the IoSR MATLAB Toolbox has been used); the numbers indicate the sample size. Stars indicate statistical significance as determined by applying the MATLAB *multcompare* function on test data derived from the MATLAB *anova1* (one-way ANOVA) function. One star denotes $p < 0.05$, two stars denote $p < 0.01$, and three stars denote $p < 0.001$. A line without a star denotes no statistically significant difference. For Figures 3J and S3H, the total length of a given error bar equals two times the square root of the number of the rescues in the corresponding bin divided by the sum of the time depolymerized in the corresponding bin.

Comparison of experimental data and model

To compare the predicted and observed timescale of Ase1 accumulation (τ) and Ase1 accumulation at steady state (A_{end}), the accumulated Ase1 as a function of time was fitted to $A_{end}(1 - e^{-t/\tau})$ in experiments and model predictions (e.g., Figure 4C for isolated MTs at 6nM of Ase1). In the model, the accumulation of Ase1 at any given timepoint is defined as $(\sum_{i=0}^{i=L} Pi) - \alpha L$. As a proxy of velocity of depolymerization at steady state, we used the average velocity of depolymerization observed after 20 s of depolymerization in experiments and compared it to the depolymerization velocity at the last simulated timepoint (Figure 4C). The 95% confidence intervals of these magnitudes were estimated using the bootstrap method. For each experimental condition with N depolymerization events, a thousand sets of N depolymerization events were drawn through sample with replacement. For each of those sets, τ and A_{end} were calculated by fitting all observations in the set, and the average velocity after 20 s was calculated. Then, the distribution of each magnitude across all sets was used to calculate the 95% confidence intervals (see source code).